

Check for updates

www.advmattechnol.de

# Single- and Double-Layer Embedded Metal Meshes for Flexible, Highly Transparent Electromagnetic Interference Shielding

Mehdi Zarei, Mingxuan Li, Ekaterini Papazekos, Yang-Duan Su, Sneh Sinha, S. Brett Walker, Melbs LeMieux, Paul R. Ohodnicki, and Paul W Leu\*

Simulation and experimental studies are carried out on single-layer and double-layer embedded metal meshes (SLEMM and DLEMM) to assess their performance as transparent electromagnetic interference (EMI) shielding. The structures consist of silver meshes embedded in polyethylene terephthalate (PET). As a transparent electrode, SLEMMs exhibit a transparency of 82.7% and a sheet resistance of 0.61  $\Omega$ sq<sup>-1</sup> as well as 91.0% and 1.49  $\Omega$ sq<sup>-1</sup>. This performance corresponds to figures of merit of 3101 and 2620, respectively. The SLEMMs achieve 48.0 dB EMI shielding efficiency (SE) in the frequency range of 8-18 GHz (X- and Ku-bands) with 91% visible transmission and 56.2 dB EMI SE with 82.7% visible transmission. Samples exhibit stable performance after 1000 bending cycles with a radius of curvature of 4 mm and 60 tape test cycles. DLEMMs consist of fabricating SLEMM on opposite sides of the substrate where the distance can be varied using a spacer. Simulations are performed to investigate how varying spacer distance between two layers of metal meshes influences the EMI SE. DLEMMs are fabricated and achieved an EMI SE of 77.7 dB with 81.7% visible transmission. SLEMMs and DLEMMs may have a wide variety of applications in aerospace, medical, and military applications.

1. Introduction

As electronic devices and systems continue to proliferate, there is a growing demand for the creation of efficient materials to

shield against electromagnetic waves. These shielding materials serve to protect electronic components against the harmful effects of radiation and prevent the interference of undesired signals.[1-7] In response to the requirements for EMI shielding, extensive research has been conducted on a diverse range of materials including metal films,[1,3,8-12] metal meshes,[9,13-19] metal nanowires,[20-22] carbon nanotubes,[23,24] graphene,[25] and MXenes.[26] Hybrid structures are also garnering increasing attention, [27-29] such as conductive oxide/ metal,[30-32] MXene/metal,[33,34] and metal/graphene.[35,36]

Furthermore, a wide array of optoelectronic devices, including LEDs, automotive windows, displays, touchscreens, and optical communication systems, require materials capable of obstructing radio frequency (RF) signals while maintaining transparency to visible light.<sup>[37–39]</sup> However, achieving this balance is

challenging. Materials like MXenes, thin films, graphene, and carbon nanotubes become less effective when transparency is a crucial requirement. In order to maintain transparency while minimizing the trade-off in shielding effectiveness (SE), [30,31,40]

M. Zarei
Department of Mechanical Engineering and Materials Science
University of Pittsburgh
Pittsburgh, PA 15260, USA
M. Li, E. Papazekos, P. W Leu
Department of Chemical Engineering
University of Pittsburgh
Pittsburgh, PA 15261, USA
E-mail: pleu@pitt.edu

V. D. S. B. B. Obdoricki

E-mail: pleu@pitt.edu
Y.-D. Su, P. R. Ohodnicki
Mechanical Engineering and Materials Science
University of Pittsburgh
Pittsburgh, PA 15260, USA

S. Sinha, S. B. Walker, M. LeMieux Electroninks Incorporated Austin, TX 78744, USA

P. R. Ohodnicki Electrical and Computer Engineering University of Pittsburgh Pittsburgh, PA 15260, USA P. W Leu

Department of Industrial Engineering University of Pittsburgh Pittsburgh, PA 15261, USA

Department of Mechanical Engineering University of Pittsburgh Pittsburgh, PA 15261, USA

The ORCID identification number(s) for the author(s) of this article can be found under https://doi.org/10.1002/admt.202302057

DOI: 10.1002/admt.202302057



236579/x, 0, Downloaded from https://ominelibrary.wiley.com/doi/10.1020/admt.202302057 by Paul Leu - University Of Pitsburgh , Wiley Online Library on [21/05/2024]. See the Terms and Conditions (https://ominelibrary.wiley.com/terms-and-conditions) on Wiley Online Library for rules of use; OA articles are governed by the applicable Creative Commons I

these materials may be paired with conductive polymers such as PEDOT:PSS<sup>[35,36]</sup> or materials with a high refractive index like indium tin oxide (ITO) or zinc oxide (ZnO).<sup>[41]</sup> In our prior work, we investigated the potential of metal thin film/metal oxide combinations for this application.<sup>[40]</sup>

As low sheet resistance is often an important factor in providing high performance EMI shielding performance, transparent electrode materials with high transparency and low sheet resistance, such as metal nanowires and metal meshes, have been the subject of much interest for transparent EMI shielding. [42–47] However, metal nanowires have challenges stemming from their uneven dispersion, inherent percolation constraints, and notable contact resistances between wires. In contrast, metal meshes tend to exhibit consistent and uniform properties, free from percolation, and contact-related concerns. [48]

In order for metal meshes to achieve high SE, a combination of small width and deep trenches is needed. [49] However, numerous manufacturing methods, such as 3D printing, crack template, and electroplating, encounter limitations in attaining widths below five micrometers.[32,50] Furthermore, controlling the width of patterns proves challenging in some methods like electroplating, crack template, and self-assembly techniques, leading to variability in pattern widths. This variability also poses a challenge for scale-up manufacturing application. Nanoimprint lithography has proven to be challenging due to demolding difficulties, achieving conformal contact, limitations in creating intricate features, and concerns regarding durability issues.<sup>[51]</sup> In contrast, photolithography is a reliable, scalable, and well-established technique for achieving uniform patterns with small width and large thickness. Lithography processes in metal applications are typically accompanied by physical vapor deposition processes such as metal evaporation or sputtering. However, these procedures tend to be costly and time-consuming, particularly when dealing with large thickness patterns.[52]

In this paper, we demonstrate a facile and scalable fabrication process to achieve embedded silver meshes in PET with small width and large thickness. Trenches are etched into the flexible PET by reactive ion etching (RIE), and reactive silver ink was employed to fill the trenches. As a transparent electrode, SLEMMs exhibit a transparency of 82.7% and a sheet resistance of 0.61  $\Omega sq^{-1}$ , as well as 91.0% and 1.49  $\Omega sq^{-1}$ . This performance corresponds to transparent electrode performance figures of merit of 3101 and 2620, respectively. Our SLEMMs achieve an average EMI SE of 56.2 dB (8 to 18 GHz) with 82.7% visible transmission and 48.0 dB EMI SE with 91.0% visible transmission. The SE was evaluated in the X- (8 to 12 GHz) and Ku-bands (12 to 18 GHz). The X-band is widely used in radar applications such as for air traffic control, weather monitoring, and military radar. The Ku-band is used for satellite communications.

Next, we studied DLEMMs. Our simulations and experiments indicate that increasing the spacer distance between two layers of metal meshes enhances the EMI SE. By incorporating a 3 mm thickness spacing to create flexible DLEMM, an EMI SE of 77.7 dB with 81.7% visible transmission was achieved. The increased spacer distance amplifies the Fabry–Pérot effect, contributing to enhanced EMI SE by enhancing the intensity of the electric field between the metal meshes and increasing absorption. Our metal meshes demonstrate the highest EMI SE performance in the literature for single-layer and double-layer metal meshes in the lit-

erature. The integration of metal meshes into PET offers a variety of advantages over glass such as flexibility, light weight, and mechanical durability. Embedded metal meshes may be utilized for a variety of optoelectronic military, medical, and aerospace applications that require high SE and high visible transparency.

#### 2. Results and Discussion

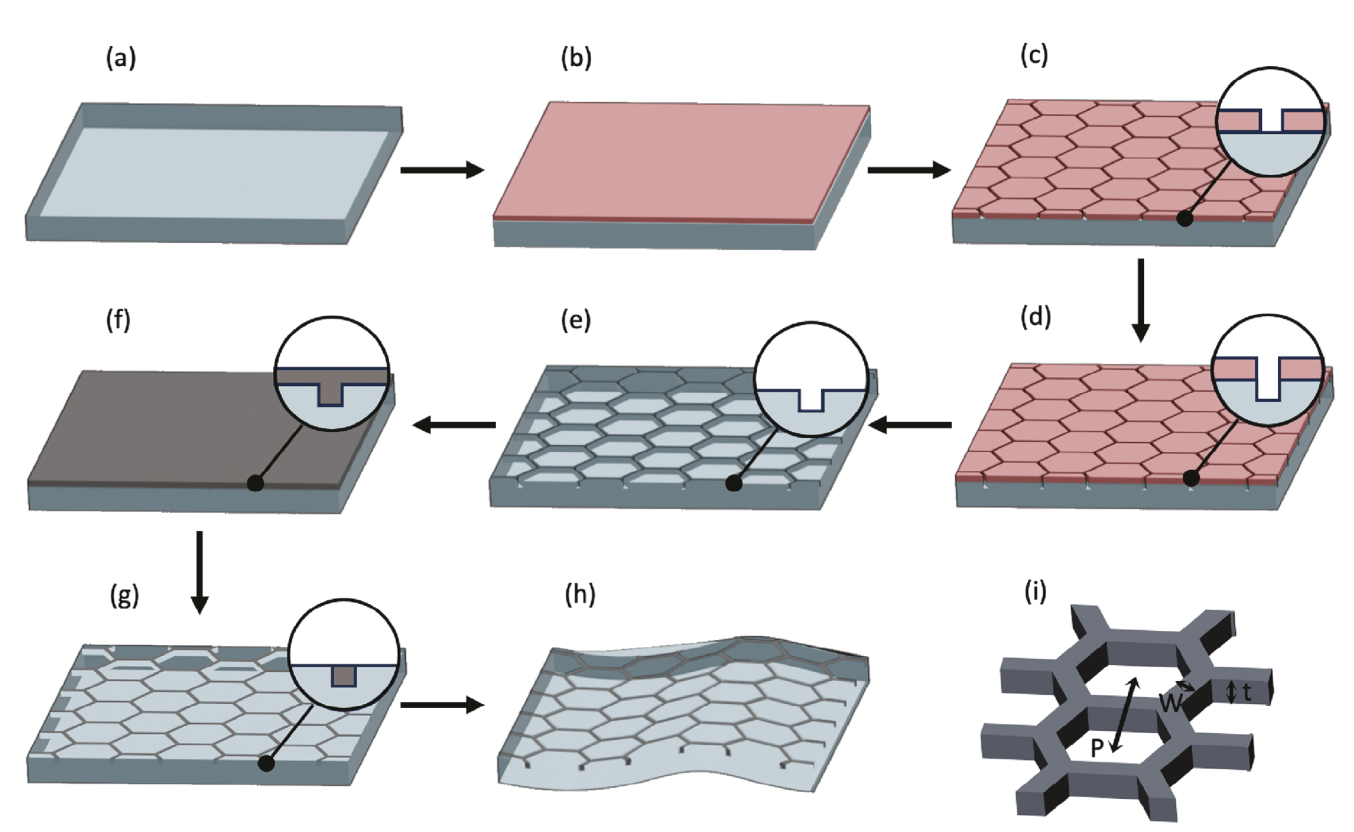
#### 2.1. Single-Layer Embedded Metal Meshes (SLEMMs)

Figure 1 depicts the schematic of the SLEMM fabrication process. A PET substrate (Figure 1a) is coated with photoresist (Figure 1b), and a hexagonal pattern is transferred to this photoresist using photolithography (Figure 1c). The hexagonal pattern is transferred into the PET substrate by RIE (Figure 1d). RIE is well-suited for etching high aspect ratio structures, such as deep trenches or narrow channels with some control over the etch depth with increasing etch time.<sup>[53]</sup> We use CF<sub>4</sub> at a flow rate of 50 sccm and SF<sub>6</sub> at 20 sccm. Then the photoresist is stripped (Figure 1e). Ag ink is coated onto the PET by drop casting and then cured at low temperatures compatible with the PET (Figure 1f). The ink is initially soft cured at temperatures ramping up from 70 to 110 °C, increasing by 10 °C every 15 min. This slow ramp process improves the filling of the trenches. The Ag ink is then hard cured at 110 °C for 30 min. Before this hard curing step, any excess Ag is removed from the sample using a cleanroom wipe. At this stage, the Ag has not fully chemically reduced into solid silver state. In addition, the binders in the silver ink have not fully cross-linked yet to provide for adhesion to the substrate. As a result of the hard cure, the Ag fully converts to its metallic solid state and firmly adheres to the underlying PET substrate. This process removes the excess silver, revealing the embedded metal meshes (Figure 1g, h). The metal meshes are defined by their width W, pitch P, and thickness t as shown in the schematic in Figure 1i. The photolithography technique we utilize is fundamentally scalable, making it well-suited for adaptation to larger production scales. Additionally, the subsequent steps in our method, including the application of Ag ink, its curing, and the removal of excess ink, are all processes that lend themselves to scalability and automation.

Two SLEMMs were fabricated, denoted as SLEMM-1 and SLEMM-2, with nominal widths (W) of 2 µm for both samples and nominal pitches (P) of 50 and 100 µm, respectively. Figure 2a shows a line-scan profile of the SLEMM-1 after etching and photoresist stripping as measured by optical profilometry. Both samples were etched for 300 s, resulting in a uniform trench thickness of 2.2 µm. The depth of the patterns can be controlled by adjusting the etch time, but the etch time is limited by the selectivity of photoresist etching. During the etching process, the photoresist layer is also etched. This introduces a limitation on the maximum etching time and, consequently, the achievable depth of the trenches. Beyond this point, further etching can lead to damage in the unprotected areas, potentially creating roughness due to the complete removal of the photoresist. This roughness provides a potential location for trapping the silver in between the meshes and reducing transparency.

Figure 2b shows a cross-sectional scanning electron microscope (SEM) image of the samples after silver filling at an 88° angle from directly overhead. This image illustrates the uniformity

23657978, Downloaded from https://oninelibrary.viley.com/doi/1.01002/adnt.202302057 by Paul Leu - University Of Pithturgh , Wiley Online Library on [21/05/2024]. See the Terms and Conditions (https://onlinelibrary.wiley.com/terms-and-conditions) on Wiley Online Library from less of use; OA articles are governed by the applicable Creative Commons License



**Figure 1.** Schematic of PET-embedded Ag meshes fabrication flow process: a) a transparent PET substrate, b) photoresist coating, c) photolithography, d) reactive-ion etching, e) photoresist stripping, f) Ag ink coating and curing, g) removal of Ag by a wiper before final curing, and finally h) the flexible PET-embedded Ag mesh. i) The Ag meshes are hexagonal arrays embedded in a PET substrate defined by width W, pitch P, and thickness t. Additionally, the schematic includes insets showing zoomed-in images of the cross-section at various fabrication stages.

and high-quality of the silver filling completed with only a single ink casting. Figure 2 displays SEM images of the (c) SLEMM-1 and (d) SLEMM-2 samples after fabrication. The SLEMM-1 and SLEMM-2 samples have measured widths of 4.0 and 3.7 µm, respectively. The measured widths are larger than the nominal widths because of sensitivity to the contact between the photomask and the substrate during exposure. The detailed information on the structural parameters of SLEMMs can be found in **Table 1.** In the top-view images (i), it is evident that the trenches are uniformly and thoroughly filled with silver, with no traces of silver between the meshes. This uniformity is advantageous, particularly for optoelectronic applications. [54] SEM images at an 82° angle from directly overhead are also shown (ii). No silver is visible in the regions in between the trenches, indicating that the wiping process effectively removes excess silver. There is some evidence of under-filling, which could be mitigated by reducing

**Table 1.** Summary of structural parameters of SLEMMs.

Sample	Nominal width [µm]	Measured width [μm]	Pitch [µm]	Measured depth [μm]
SLEMM-1	2	4.0	50	2.2
SLEMM-2	2	3.7	100	2.2

the width of the trenches. In general, narrower trenches tend to achieve better filling compared to wider ones. During the Ag ink curing process, there is a large reduction in volume due to evaporation. However, the surface tension in the aqueous silver ink enables it to bulge over the top edge of the trench, resulting in smaller width trenches with less under-filling.

**Figure 3** illustrates the comparative performance of our SLEMMs with other flexible metal meshes serving as transparent electrodes. Figure 3a shows the transmission T at a wavelength of 550 nm versus sheet resistance  $R_s$ . The SLEMM-1 and SLEMM-2 samples have transmissions of 82.7% and 91%, respectively, with  $R_s$  of 0.61 and 1.49, respectively. Figure 3b plots  $\sigma_{DC}/\sigma_{OP}$  for the two metal meshes as a function of  $R_s$  compared with other works from the literature.  $\sigma_{DC}/\sigma_{OP}$  is a metric employed to assess transparent electrodes, calculated as the ratio between their direct current conductivity ( $\sigma_{DC}$ ) and optical conductivity ( $\sigma_{OP}$ ). A higher figure of merit signifies a more efficient device capable of transmitting greater electrical current while preserving excellent optical transparency. The figure of merit is related to T and  $R_s$  by:

$$\frac{\sigma_{DC}}{\sigma_{OP}} = \frac{Z_0}{2R_s} \frac{\sqrt{T}}{1 - \sqrt{T}} \tag{1}$$

where  $Z_0 = 377~\Omega$  is the free space impedance. The SLEMM-1 and SLEMM-2 samples achieve  $\sigma_{DC}/\sigma_{OP}$  of 3100 and 2620,

2365798x, 0, Downloaded from https://onlinelibrary.wiley.com/doi/10.1002/admt.202302057 by Paul Leu - University Of Pittsburgh , Wiley Online Library on [21/05/2024]. See the Terms and Conditions (https://onlinelibrary.wiley.com/errms-and-conditions) on Wiley Online Library for rules of use; OA articles are governed by the applicable Creative Commons License

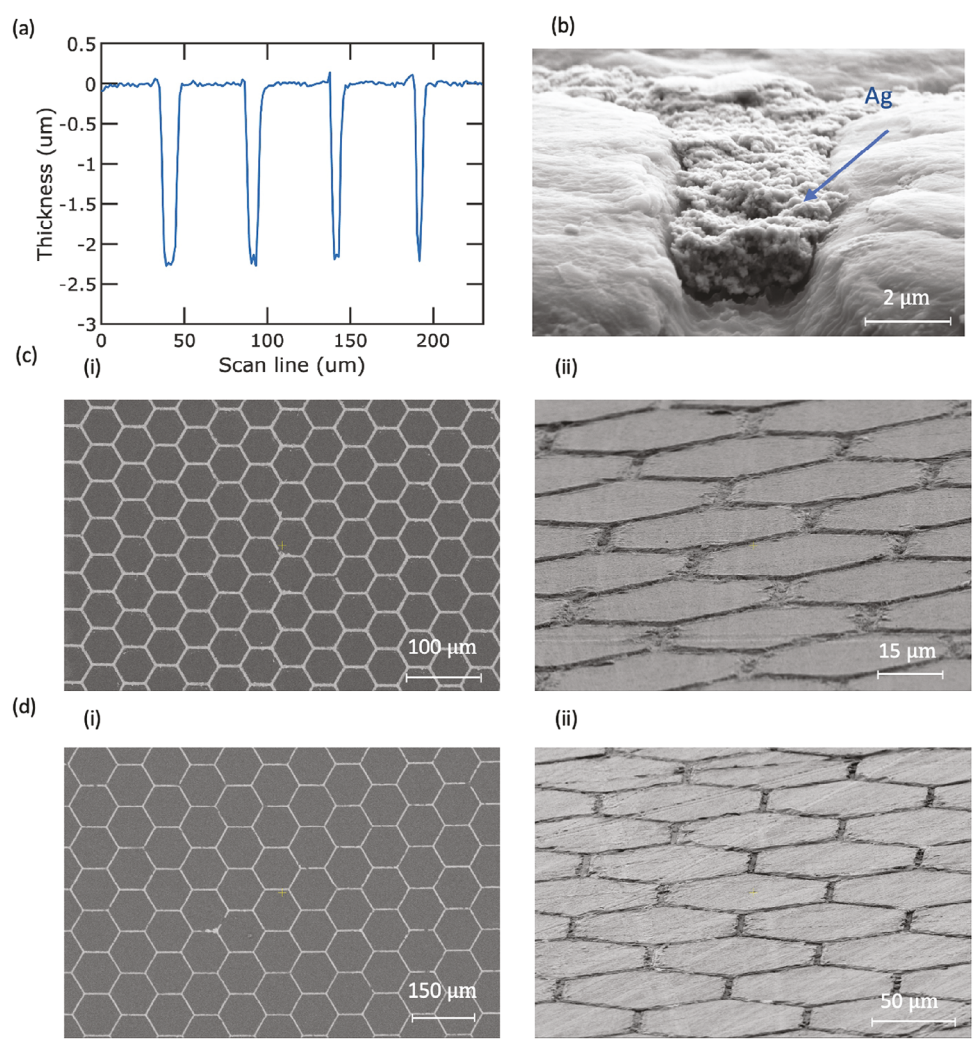


**Figure 2.** Structural characterization of SLEMMs. a) Optical profilometry measurement of SLEMM-1 sample after etching. The trench depths of both the SLEMM-1 and SLEMM-2 samples are the same. b) cross-sectional scanning electron microscopy (SEM) image showing Ag filling of the trenches at an  $88^{\circ}$  angle from directly overhead with an actual width of  $3.7\mu$ m. SEM images of (c) SLEMM-1 and (d) SLEMM-2 samples, captured from (i) top view and (ii) at  $82^{\circ}$  angle from directly overhead.

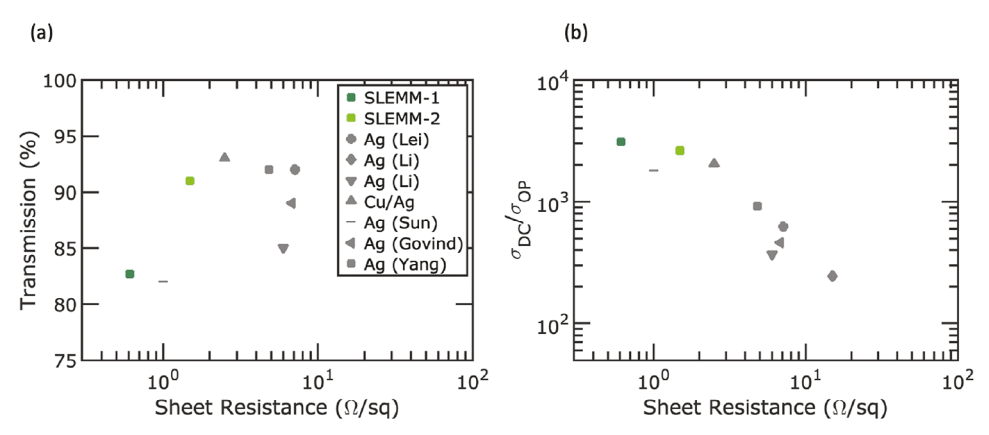


**Figure 3.** A performance comparison between our SLEMMs and other flexible metal meshes in the literature. a) transmission versus sheet resistance and b) figure of merit  $\sigma_{DC}/\sigma_{OP}$  versus sheet resistance. The following works from the literature are included: Ag mesh (Lei),<sup>[55]</sup> Ag mesh (Li),<sup>[50]</sup> Ag mesh (Li),<sup>[50]</sup> Ag mesh (Sovind),<sup>[58]</sup> and Ag mesh (Yang).<sup>[59]</sup>

2365709x, 0, Downloaded from https

:/onlinelibrary.wiley.com/doi/10.1002/admt.202302057 by Paul Leu - University Of Pitsburgh , Wiley Online Library on [21/05/2024]. See the Terms and Conditions (https://onlinelibrary.wiley.com/terms/

-conditions) on Wiley Online Library for rules of use; OA articles are governed by the applicable Creative Commons I

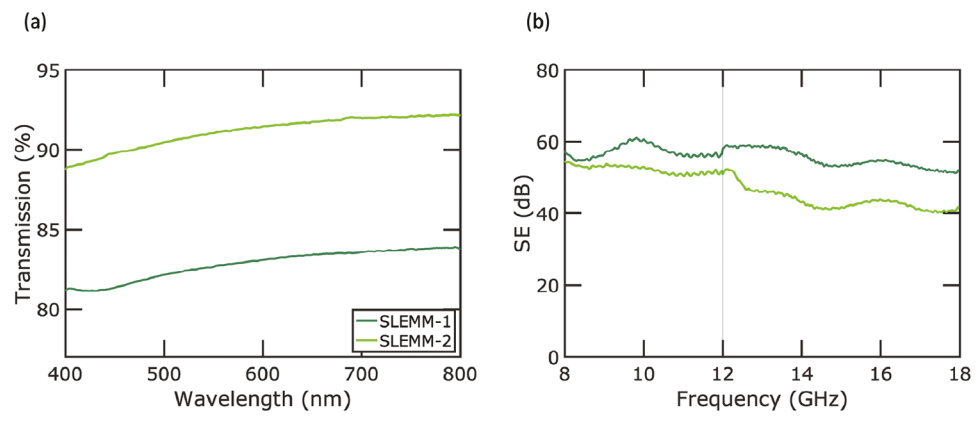


Figure 4. a) Transmission versus wavelength and b) EMI SE versus frequency in the range of 8–18 GHz for SLEMMs. The transmission wavelengths covers the visible range. The frequency range shown covers the X- (8–12 GHz) and Ku-bands (12–18 GHz).

respectively. The superior performance of our samples indicates that our fabrication method is capable of creating highly transparent and conductive metal meshes, which is beneficial for numerous optoelectronic applications. Table S1 (Supporting Information) provides details of the comparison between our samples and other flexible metal meshes in the literature as transparent electrodes.

Figure 4a displays the optical transmission results in the visible wavelength range of 400 to 800 nm. The transmission measurements were adjusted to remove the influence of the substrate, meaning that the final reported transmission values were calculated by dividing the initially measured transmission by the transmission of the substrate. A higher pitch results in a higher transmission, as there is more non-mesh space for light to pass through. However, this rise in transmission corresponds to a decrease in SE, as shown in Figure 4b. A balance must be achieved between SE and T. For the same metal mesh width and thickness, an increase in pitch leads to a decrease in SE. For the same pitch and width, increasing thickness enhances both conductance and SE while maintaining constant transmission. However, fabricating deeper trenches than what was achieved in this work is not possible due to etching of the photoresist discussed earlier. The SLEMM-1 and SLEMM-2 samples achieve an average EMI SE of 56.2 and 48.0 dB, respectively. The contribution of SE from reflection  $SE_R$  and absorption  $SE_A$  for each sample is detailed in Figure S1a (Supporting Information) and the total reflection, absorption, and transmission are shown in Figure S1b (Supporting Information). This figure indicates that the reflection loss is about the same across all samples at  $SE_R$  of about 13 dB and the meshes reflect about 95% of incident energy. The primary difference in performance for the samples comes from differences in  $SE_A$ . The theoretical transmission of the metallic metal mesh is estimated by calculating the ratio of open area between the metal mesh to the total surface area. Table 2 provides a comparison of the simulation and experimental measurement for T, SE, and  $R_{\rm s}$  of the fabricated samples. Simulations were previously used to highlight the importance of minimizing the width of metal meshes and maximizing their thickness in order to improve EMI shielding performance. [49] High frequency electromagnetic field simulations using the finite element method were used to predict EMI SE performance. A conductivity of 20% of bulk Ag conductivity was used in simulations based on experiments with Ag thin films (Figure S2, Supporting Information). The sheet resistance was simulated from the finite element method and the simulated transparency was calculated based on the fraction of open area between the metal meshes. Good agreement can be seen between the simulation and experimental results for the two samples.

PET-embedded metal meshes offer flexibility, which may be applicable for flexible electronics, roll-up displays, or wearable devices. Surface-sputtered metal meshes often encounter adhesion issues, which can lead to poor performance in bending tests. In contrast, the embedded structures exhibit improved adhesion, contributing to their superior bending test results. To evaluate the mechanical durability of the embedded metal mesh samples in flexible optoelectronics, we conducted bending and tape tests to assess the mechanical performance of the manufactured metal meshes. Figure 5a plots the outcomes of the bending tests. After every 100 bending cycles, we measured and recorded the absolute sheet resistance. The bending radius used was 4 mm, and the samples were subjected to bending under tension. Each cycle represents one cycle of tension and tension release from the sample. The inset figures show the relative sheet resistance enhancement for both samples. After 1000 cycles, the SLEMM-1 sample showed a sheet resistance increase from 0.6 to 0.8  $\Omega$ sq<sup>-1</sup>, while the SLEMM-2 sample exhibited a sheet resistance increase from 1.5 to 1.8  $\Omega$ sq<sup>-1</sup>. After the bending test, a 3M Scotch tape test was applied to the samples (Figure 5b). After 60 cycles, the SLEMM-1 sample showed a sheet resistance increase from 0.8 to 0.9  $\Omega$ sq<sup>-1</sup>, while the SLEMM-2 sample exhibited a sheet resistance increase

**Table 2.** Summary of the simulation and experiment performance for SLEMMs.

Sample		Simulatio	ns		Experiments		
	Т	SE	R <sub>s</sub>	Т	SE	R <sub>s</sub>	
	[%]	[dB]	$\overline{[\Omega sq^{-1})}$	[%]	[dB]	$[\Omega sq^{-1}]$	
SLEMM-1	84.6	55.3	0.29	82.7	56.2	0.61	
SLEMM-2	92.7	51.6	0.34	91.0	48.0	1.49	

2365709x, 0, Downloaded from https://onlinelibrary.wiley.com/doi/10.1002/admt.202302057 by Paul Leu - University Of Pittsburgh , Wiley Online Library on [21/05/2024]. See the Terms and Conditions (https://onlinelibrary.wiley.com/erms

and-conditions) on Wiley Online Library for rules of use; OA articles are governed by the applicable Creative Commons I

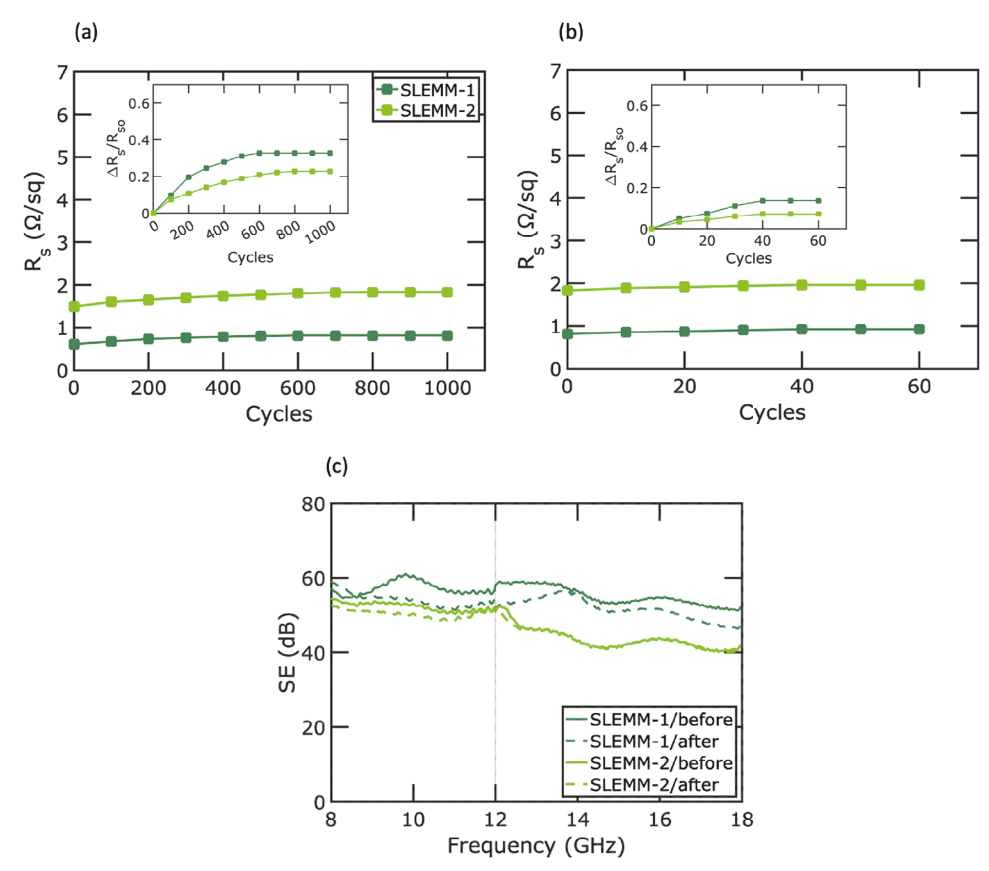


Figure 5. Sheet resistance change of SLEMMs under (a) bending test and (b) tape test with varying number of cycles. (c) EMI shielding efficiency comparison before and after the application of both tests.

from 1.8 to  $2.0 \,\Omega sq^{-1}$ . The observed changes in sheet resistance, both after the bending test and the subsequent tape test, were found to be relatively small, indicating that the samples exhibited robust performance under these rigorous tests, with no significant impact on their overall functionality. To ensure that the bending and tape tests did not have a significant effect on the EMI SE performance of the samples, SE measurements were taken after both tests (Figure 5c). For the SLEMM-1 samples, the average SE decreased from 56.2 to 52.8 dB. Similarly, the SLEMM-2 samples exhibited a slight decrease from 48.0 to 46.9 dB. This slight decrease in EMI SE is attributed to the slight increase in sheet resistance. To ensure that the microstructure of the samples did not change during those tests, we captured top-view SEM images of the samples after the tests, and the results have been included in Figure \$3 (Supporting Information). By comparing SEM images before the tests (Figure 2) with SEM images after the tests (Figure S3, Supporting Information), no alterations in microstructure, cracking, or segmentation of Ag meshes were ob-

In **Figure 6**, we compare the EMI SE and transmission performance of our fabricated SLEMMs with other single-layer flexible metal mesh EMI shielding in the literature. Literature works includes Ag mesh (Zarei),<sup>[60]</sup> Ag/Cu mesh,<sup>[61]</sup> ZnO/Ag/ZnO,<sup>[31]</sup> ITO/Cu-doped/ITO,<sup>[30]</sup> Cu mesh (Walia),<sup>[62]</sup> Cu mesh (Liao),<sup>[63]</sup> Ag mesh (Voronin),<sup>[64]</sup> Ag mesh (Kim),<sup>[65]</sup> Ag mesh (Lei),<sup>[55]</sup> Ag mesh (Li),<sup>[50]</sup> and Cu mesh (Voronin),<sup>[66]</sup> It should be noted that

different research papers explore a wide range of frequencies and present SE values in different ways, such as maximum, minimum, or average. However, for consistency with this paper, we report the average SE within the 8–18 GHz range. Additional information regarding the comparison of our results with other

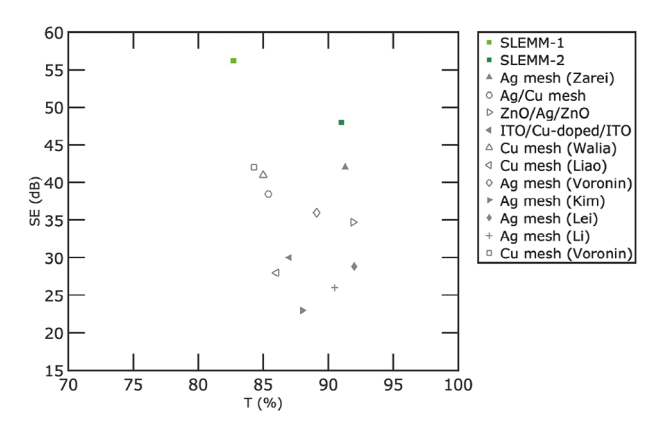


Figure 6. Comparison of the EMI SE (dB) and transmission (at 550 nm) of our SLEMMs with other single-layer flexible metal meshes in the literature. The works from literature include Ag mesh (Zarei), [60] Ag/Cu mesh, [61] ZnO/Ag/ZnO, [31] ITO/Cu-doped/ITO, [30] Cu mesh (Walia), [62] Cu mesh (Liao), [63] Ag mesh (Voronin), [64] Ag mesh (Kim), [65] Ag mesh (Lei), [55] Ag mesh (Li), [50] and Cu mesh (Voronin). [66]

2365709x, 0, Downloaded from https://onlinelibrary.wiley.com/doi/10.1002/admt.202302057 by Paul Leu - University Of Pittsburgh , Wiley Online Library on [21/05/2024]. See the Terms and Conditions (https://onlinelibrary.wiley.com/terms

and-conditions) on Wiley Online Library for rules of use; OA articles are governed by the applicable Creative Commons I

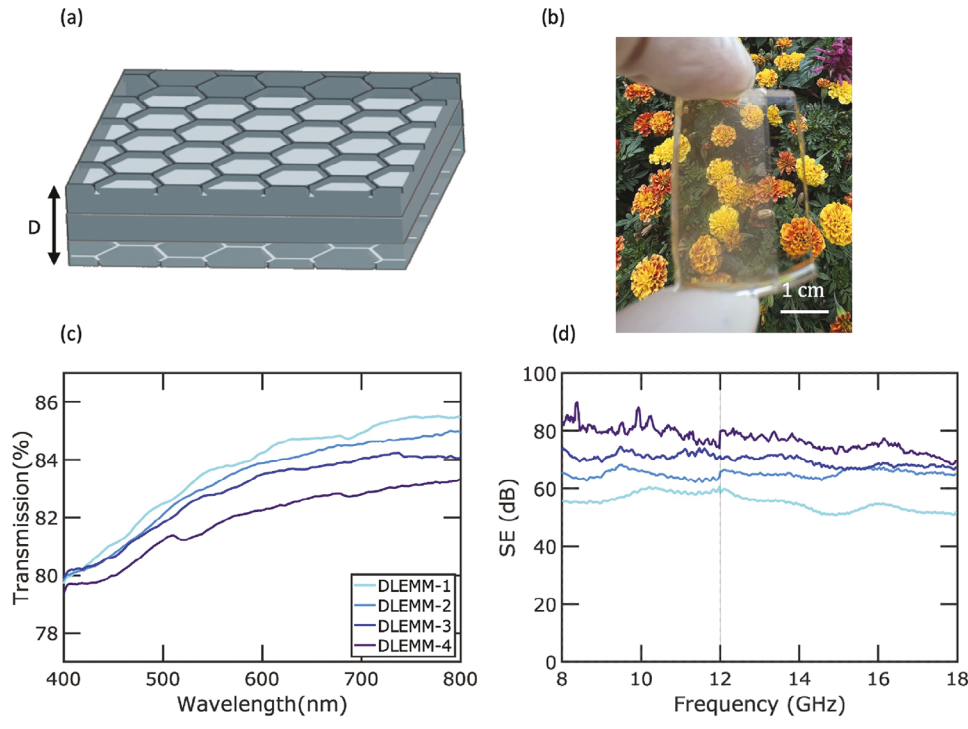


Figure 7. Characterization and EMI performance of DLEMMs. a) Schematic of DLEMM structure with a spacer distance between two mesh layers. Please note that D is given in units of mm as opposed to W and P, which are listed in  $\mu$ m. b) Optical image of SLEMM-2/D3.25 sample with 81.7% transmission at 550 nm with a PDMS spacer larger than the mesh layers. c) Transmission versus wavelength for different DLEMMs with increasing spacer thickness d) EMI SE versus frequency in the range of 8–18 GHz for four DLEMMs with increasing thickness D.

studies works in literature can be found in Table S2 (Supporting Information).

Our samples outperform other works in the literature due to the small mesh width, large mesh depth, uniformity, and connectivity of the mesh, along with the use of Ag ink, which provides higher conductivity compared to other metals and composite materials. In general, a small width and large thickness are key factors in achieving a higher SE with metal mesh structures. However, it's worth noting that most of the metal meshes manufactured to date have widths exceeding 5 µm. Additionally, commonly employed 3D printing techniques like inkjet, gravure, screen, and flexography tend to produce line widths greater than 10 µm. Producing metal meshes with substantial thickness poses its own unique challenges. Electroplating and electrodeposition methods offer potential solutions for increasing the thickness of metal meshes. Nevertheless, these methods come with their limitations, including the tendency for metal to deposit isotropically, leading to an unintentional increase in width. Additionally, the process of achieving a sputtered Ag thickness of up to 2.5 µm is highly time-consuming and not suitable for scalable large-area fabrication.<sup>[64]</sup> Here, we demonstrate a record performance for transparent EMI shielding on a flexible substrate.

#### 2.2. Double-Layer Embedded Metal Meshes (DLEMMs)

We next focused our attention on DLEMMs. Flexible DLEMMs have previously been studied with Ag meshes by crack lithography,<sup>[64]</sup> Ag meshes by nanoimprint lithography,<sup>[51]</sup> Ni

meshes by nanoimprint lithography,<sup>[67]</sup> and multi-layer silver/metal oxides by deposition.<sup>[31]</sup> By applying multiple layers of metal meshes, the SE may be increased while maintaining an acceptable optical transparency. The enhanced SE results from the attenuation of the radio wave through the Ag meshes as well as the multiple internal reflections between the metal meshes.

We investigate how varying the distance between the Ag mesh layers affects the EMI SE performance. **Figure 7a** shows the schematic of structures studied, which consists of two Ag mesh layers on opposite sides of the substrate where the total thickness between the Ag meshes is D. Four different flexible DLEMMs with varying thicknesses were evaluated, corresponding to thickness values D of 0.25, 1.25, 2.25, and 3.25 mm. We refer to these samples as DLEMM-1, DLEMM-2, DLEMM-3, and DLEMM-4, respectively. Please note that D is given in units of mm as opposed to the metal mesh width W and pitch P, which are both given in units of  $\mu$ m. Two SLEMMs of SLEMM-2 were used to fabricate the DLEMM structures, since they have a higher transparency than the SLEMM-1 samples and we expect the transparency to decrease when creating double-layer metal meshes. The PET substrate has a thickness of 0.125 mm.

The DLEMM-1 consists of stacking two single layers of metal meshes back to back. To achieve larger thicknesses *D*, we used polydimethylsiloxane (PDMS) as spacers between the two SLEMMs. In the case of DLEMM-2, DLEMM-3, and DLEMM-4 samples, two single layers of metal meshes were affixed to opposite sides of a PDMS spacer with varying thicknesses of 1, 2, and 3 mm, respectively. Figure 7b shows an optical image of the DLEMM-4 sample with 81.7 % transmission at 550 nm. The

2365709x, 0, Downloaded from https

//onlinelibrary.wiley.com/doi/10.1002/adnt1020302057 by Paul Leu - University Of Pittsburgh , Wiley Online Library on [21/05/2024]. See the Terms and Conditions (https://onlinelibrary.wiley.com/terms-and-conditions) on Wiley Online Library for rules of use; OA articles are governed by the applicable Ceative Commons I

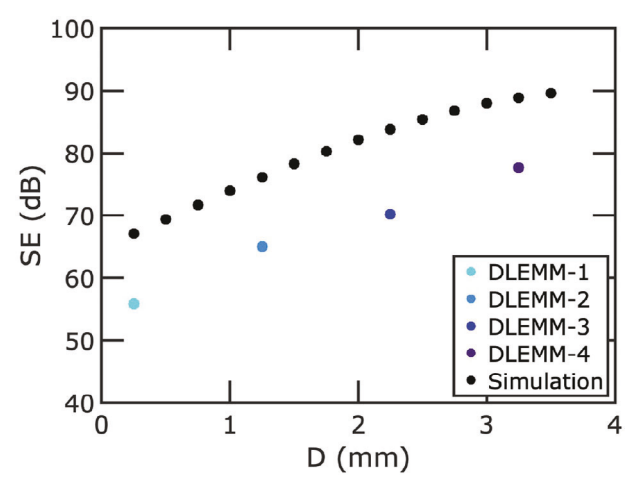


**Figure 8.** High frequency electromagnetic field simulation results of DLEMMs with different total thicknesses *D* compared to experimental results. Simulation results are shown with black circles and experimental results are plotted in colored circles.

PDMS spacer is larger than the two metal mesh layers attached to both sides, and its transparency is visible in the right portion of the sample. Figure 7c displays the transmission for DLEMM samples within the visible wavelength range. In all reported transmission measurements, the substrate contribution was excluded. The reduction in transmission with increasing thickness may be due to the haze in the metal meshes, where light is scattered due to imperfections in the mesh such as roughness of surfaces. However, the influence of thickness on SE is considerably more pronounced (Figure 7d). By increasing the sample thickness, SE increases significantly. The improvement in SE by increasing the thickness is primarily due to an increase in SE<sub>4</sub> as SE<sub>P</sub> remains approximately constant (Figure S4, Supporting Information). There is no strict limit to fabricating thicker PDMS thicknesses; however, it is important to note that a thicker PDMS results in a less flexible substrate as the bending stiffness of the material is proportional to  $D^3$ .

To better understand the increase in SE performance in DLEMMs, we conducted simulations with varying thickness between two metal mesh layers. Figure 8 presents the simulation results and compares them to our experimental results for the DLEMMs of varying total thicknesses D. Good agreement can be seen between the simulation and experimental results. The fabricated flexible DLEMM samples underperform simulations, likely due to underfilling of the trenches as discussed earlier. Simulations for the SLEMM-2 predict an SE of 51.6 dB with a transparency of 92.7%. In contrast, the DLEMMs have an SE from 67.1 to 88.9 dB with increasing thickness from 0.25 to 3.25 mm. A maximum SE of 86.7 dB is observed at a total thickness of 5.6mm (Figure S5, Supporting Information), though these samples were not fabricated as such large thickness samples tend to suffer from increasing leakage and noise from the environment through the sides of the sample.

The large improvement in SE in the DLEMM samples compared to the SLEMM samples is due to the Fabry-Pérot effect. In our DLEMMs, the Fabry-Pérot effect is particularly relevant for the frequency band of 8-18 GHz. For this frequency range,

Table 3. Summary of the EMI performance of the DLEMMs.

Sample	DistanceD	Simulations		Experiments	
	[mm]	Т	SE	Т	SE
		[%]	[dB]	[%]	[dB]
DLEMM-1	0.25	85.0	67.1	83.8	55.8
DLEMM-2	1.25	85.0	76.1	83.1	65.0
DLEMM-3	2.25	85.0	83.9	82.8	70.2
DLEMM-4	3.25	85.0	88.9	81.7	77.7

the first-order harmonic peak of resonance occurs at cavity thicknesses between 4.2 and 9.4 mm. Since the thicknesses we are exploring in DLEMMs are all below 4 mm, an increase in thickness moves the structure closer to the first-order harmonic peak. The structures exhibit an increase in  $SE_A$  and thus, SE. As the thickness of the spacer between the two metal meshes increases, our structure approaches the optimal condition for the first-order resonance, leading to a more pronounced absorption and improved SE within this specific frequency band. Simulation for a longer range of D are shown in Figure \$5 (Supporting Information), where a maximum SE may be observed around D = 5.5 mm. The effect may be exploited in EMI shielding applications as it is particularly significant at radio frequencies.[31,68,69] The Fabry-Pérot effect augments SE through multiple reflections between the two metal meshes, leading to increased absorption. Figure S1 (Supporting Information) shows the shielding contribution of reflection and absorption for all the samples fabricated in this study. Since the reflection values for DLEMM structures are similar to those of SLEMM samples, the primary reason for a higher SE value in these structures is the increased absorption due to multiple reflections. The radio waves are trapped between the two single-layer metal meshes and thus absorption is enhanced.

**Table 3** provides details of T and SE on the DLEMM structures. Good agreement can be seen between the simulation and experimental results. The transmission T for the DLEMMs are calculated by assuming that the metal meshes are not aligned and instead offset by a random shift in the x – and y – direction with uniform probability. The visible transparency is then estimated based on the fraction of area that is not blocked by the metal mesh.

In **Figure 9**, we compare the EMI SE performance and transmission of our flexible DLEMMs with other double-layer flexible transparent metal meshes in the literature. Literature works includes ZnO/Ag/ZnO,<sup>[31]</sup> Ag mesh,<sup>[64]</sup> and Ni mesh.<sup>[67]</sup> Similar to the single-layer comparison, we used the same consistency for reporting SE and transmission. Additional information regarding the comparison of our results with other works can be found in Table **S2** (Supporting Information). A higher performance in our single-layer metal meshes can be further enhanced in double-layer metal meshes.

#### 3. Conclusion

Our fabrication approach allowed us to create single- and doublelayer metal meshes embedded in PET with narrow widths and large thicknesses. We utilized reactive silver ink for filling

2365798x, 0, Downloaded from https://onlinelibrary.wiley.com/doi/10.1002/admt.202302057 by Paul Leu - University Of Pitisburgh , Wiley Online Library on [21/05/2024]. See the Terms and Conditions (https://onlinelibrary.wiley.com/errms

and-conditions) on Wiley Online Library for rules of use; OA articles are governed by the applicable Creative Commons I

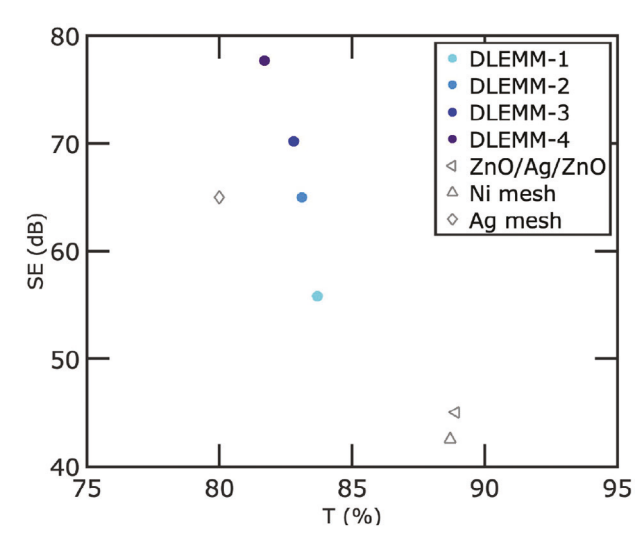


Figure 9. Comparison of the EMI SE (dB) and transmission (at 550 nm) of our DLEMMs with other flexible double-layer metal meshes in the literature: ZnO/Ag/ZnO,[31] Ag mesh,[64] and Ni mesh.[67]

the meshes, circumventing the need for expensive machinery. Through simulations, we identified that increasing the spacer distance between layers of metal mesh enhances SE. Our experimental results showcase the excellent EMI SE and transparency of these structures. As a transparent electrode, SLEMMs exhibit a transparency of 82.7% and sheet resistance of 0.61  $\Omega sq^{-1}$ , as well as 91.0% and 1.49  $\Omega sq^{-1}$ . This performance corresponds to figures of merit of 3101 and 2620, respectively. Our SLEMMs achieve 48.0 dB EMI SE with 91% visible transmission and 56.2 dB EMI SE with 82.7% visible transmission. These flexible metal mesh-embedded substrates hold great promise for a wide range of optoelectronic applications, owing to their remarkable transparent EMI shielding capabilities achieved through the combination of high-conductivity of silver, small widths, and large thicknesses.

#### 4. Experimental Section

Ink Information: Commercially available EI-1201, an Ag metal-complex based conductive inks from Electroninks Inc, was used in this study. The ink was derived from a formulation previously developed by one of the authors.  $[^{70}]$  In these inks, the ammonia ligands compounds act as a stabilizer. When the ink was cured in an oven, the liable ammonia ligands compounds evaporate and the Ag compound was reduced to form Ag. Figure S2 (Supporting Information) shows the characterization of  $R_s$  against Ag film thickness of this grade of ink.

Fabrication of PET-Embedded Ag Mesh: The process for fabricating Ag meshes embedded in PET is illustrated in Figure 1. PET sheets (MELINEX ST505) were Purchased from Tekra Inc., with a thickness of 125  $\mu m$ . The sheets were trimmed into 30 mm  $\times$  30 mm samples using a scissor. Subsequently, these samples underwent ultrasonic cleaning in acetone, methanol, and isopropyl alcohol (IPA), each for a duration of 10 min. Finally, they were dried using nitrogen gas. To enhance the adhesion of the photoresist to the PET, HMDS was sputtered onto the substrate using a vapor prime oven system. Subsequently, a layer of AZ4110 photoresist was spin-coated onto the substrate at a spin speed of 2500 rpm, resulting in a thickness of 1.5  $\mu m$ . All samples were baked at 98 °C for 4 min. Patterns were made on the photoresist using the Quintel Q4000 MA Mask Aligner with UV light exposure, and were developed for

2 min in AZ400 K (1:4) (from MicroChemicals). Reactive ion etching (RIE) was used to transfer the patterns to the PET with a gas flow of 50 sccm CF<sub>4</sub> and 20 sccm SF<sub>6</sub>, a pressure of 30 mT, and a power of 250 W. The depth of the patterns could be controlled by adjusting the etch time, but there was a limitation as the photoresist also gets etched during the process. Once the photoresist was completely etched, it could damage the PET substrate by creating some roughness, which may trap silver and reduce transmission. Therefore, the maximum achievable etch time for 1.5  $\mu m$  thickness of the photoresist was utilized. An etch time of 300 s was selected, resulting in a depth of 2.2 µm, as obtained from optical profilometry measurement. The photoresist was removed from the sample by ultrasonication in acetone, methanol, and IPA, each for 10 min. Then, the samples were dried using nitrogen gas. Particle-free silver ink (EI-1201 from Electroninks) was drop-cast on the samples. The reactive silver ink was filtered through a 0.22 μm syringe filter to eliminate large particles prior to drop casting. Flexible PET substrates were weighted at the edges to ensure flatness of the samples. Due to its low surface tension, the silver ink effectively wets the surface uniformly. For a 30 mm × 30 mm sample size, 1.7 g of ink was drop-cast to ensure sufficient ink for proper filling of trenches. Samples were ramp-cured starting at 70 °C with a step increase of 10 °C every 15 min. The final curing temperature was set at 110 °C. Prior to the hard curing process, Ag was wiped off the sample using a cleanroom wiper following the soft curing of Ag. Subsequently, a final curing step lasting 30 min was carried out to ensure the complete curing of Ag. The samples were then spray-washed with acetone, methanol, and IPA to remove any Ag particulates. To create different PDMS thicknesses, Dow SYLGARD 184 Silicone Elastomer was used. This material is a twocomponent solution with a mixing ratio of 10:1. After mixing in a petri dish, a pump was used to remove the bubbles created during mixing and then cured it at 60 °C for 2 h. After peeling of the PDMS from the petri dish, UV glue was used to attach two metal mesh layers to both sides of the PDMS.

Characterization: A probe station with a semiconductor device analyzer (B1500A Semiconductor Device Analyzer from Keysight Technologies) was used to measure sheet resistance via the van der Pauw method. To get a high resolution images of the embedded Ag meshes, scanning electron microscopy (Zeiss SIGMA VP) was employed. The total transmittance was measured over the wavelength range of 400 to 800 nm using a UV-vis-NIR spectrometer with a 60 mm diameter integrating sphere (JASCO Spectrophotometer V-770). The transmission values reported in this study were calculated by excluding the effect of the substrate transmission. To achieve this, the measured transmission values were divided by the substrate transmission. A 3D Optical Profilometer (Bruker) was used to measure the depth of the etched samples. The electromagnetic interference shielding effectiveness (EMI SE) was determined using the coaxial transmission line method, with the aid of an HP 7822D Vector Network Analyzer (VNA) for signal generation and detection. The sample was positioned between two waveguide flanges, with the appropriate flange chosen based on the desired frequency range. The waveguide flanges were secured in place using screws and nuts to prevent any shifting during the measurement. The X band and Ku band waveguide flanges were obtained from Pasternack. The data was smoothed using a weighted average around five neighboring points for the double-layer meshes

Simulations: EMI shielding performance was simulated using the Ansys High Frequency Structure Simulator (HFSS). HFSS utilizes the finite element method to solve Maxwell's equations. The simulated transparency of the metal meshes was approximated by calculating the fraction of open area between the metal meshes based on their pitches and measured widths. The sheet resistance was simulated in Comsol finite element analysis, where the conductivity of the silver was assumed to be 20% of that of bulk conductivity.

### **Supporting Information**

Supporting Information is available from the Wiley Online Library or from the author.

# ADVANCED MATERIALS TECHNOLOGIES

2365/90x, D. Downloaded from https://onlinelibrary.wiely.com/doi/10.1002/admt.203202057 by Paul Leu - University Of Fitsburgh , Wiley Online Library on [21/05/2024]. See the Terms and Conditions (https://onlinelibrary.wiely.com/berms-and-conditions) on Wiley Online Library for rules of use. OA articles are governed by the applicable Centative Commons.

# Acknowledgements

The authors acknowledged support from the MDS-Rely Center to conduct this research. The MDS-Rely Center was supported by the National Science Foundation's Industry—University Cooperative Research Center (IUCRC) Program under award EEC-2052662 and EEC-2052776.

#### **Conflict of Interest**

The authors declare no conflict of interest.

# **Data Availability Statement**

The data that support the findings of this study are available on request from the corresponding author. The data are not publicly available due to privacy or ethical restrictions.

# **Keywords**

EMI shielding, flexible transparent conductive electrode, metal ink, metal mesh, photolithography, reactive ion etching (RIE)

Received: November 30, 2023 Revised: January 30, 2024 Published online:

- M. Li, S. Sinha, S. Hannani, S. B. Walker, M. LeMieux, P. W. Leu, ACS Appl. Electron. Mater. 2023, 5, 20591.
- [2] Y. Bhattacharjee, S. Bose, ACS Appl. Nano Mater. 2021, 4, 949.
- [3] M. Li, M. Zarei, A. J. Galante, B. Pilsbury, S. B. Walker, M. LeMieux, P. W. Leu, Prog. Org. Coat. 2023, 179, 107506.
- [4] X.-Y. Wang, S.-Y. Liao, Y.-J. Wan, P.-L. Zhu, Y.-G. Hu, T. Zhao, R. Sun, C.-P. Wong, J. Mater. Chem. C 2022, 10, 44.
- [5] A. J. Galante, M. Li, B. Pilsbury, M. LeMieux, Q. Liu, P. W. Leu, ACS Appl. Polym. Mater 2022, 4, 5253.
- [6] Y. Zhan, C. Santillo, Y. Meng, M. Lavorgna, J. Mater. Chem. C 2023, 11, 859.
- [7] C. Liang, Z. Gu, Y. Zhang, Z. Ma, H. Qiu, J. Gu, Nano-Micro Lett. 2021, 13. 181.
- [8] Z. Li, H. Li, X. Zhu, Z. Peng, G. Zhang, J. Yang, F. Wang, Y.-F. Zhang, L. Sun, R. Wang, Z. Jinbao, Y. Zhongming, Y. Hao, L. Hongbo, Adv. Sci. 2022, 9, 2105331.
- [9] H. Li, Z. Li, N. Li, X. Zhu, Y.-F. Zhang, L. Sun, R. Wang, J. Zhang, Z. Yang, H. Yi, X. Xiaofeng, L. Hongbo, Small 2022, 18, 2107811.
- [10] Q.-M. He, J.-R. Tao, D. Yang, Y. Yang, M. Wang, Chem. Eng. J. 2023, 454, 140162.
- [11] H. Wang, D. Zheng, Y. Zhang, L. Han, Z. Cao, Z. Lu, J. Tan, ACS Appl. Mater. Interfaces 2023, 15, 49487.
- [12] S. J. DiGregorio, S. Raikar, O. J. Hildreth, ACS Appl. Electron. Mater. 2023, 6, 203.
- [13] X. Lu, Y. Zhang, Z. Zheng, Adv. Electron. Mater. 2021, 7, 2001121.
- [14] V. H. Nguyen, D. T. Papanastasiou, J. Resende, L. Bardet, T. Sannicolo, C. Jiménez, D. Muñoz-Rojas, N. D. Nguyen, D. Bellet, *Small* 2022, 18, 2106006.
- [15] H. B. Lee, W.-Y. Jin, M. M. Ovhal, N. Kumar, J.-W. Kang, J. Mater. Chem. C 2019, 7, 1087.
- [16] Z. Zhou, S. B. Walker, M. LeMieux, P. W. Leu, ACS Appl. Electron. Mater. 2021, 3, 2079.
- [17] X. Zhu, M. Liu, X. Qi, H. Li, Y. Zhang, Z. Li, Z. Peng, J. Yang, L. Qian, Q. Xu, N. Gou, J. He, D. Li, H. Lan, Adv. Mater. 2021, 33, 2007772.

- [18] Y. Liang, X. Huang, K. Wen, Z. Wu, L. Yao, J. Pan, W. Liu, P. Liu, Appl. Sci. 2023, 13, 4846.
- [19] S.-i. Chung, P. K. Kim, T.-g. Ha, J. Micromech. Microeng. 2023, 33, 035002.
- [20] Y. Xing, Y. Wan, Z. Wu, J. Wang, S. Jiao, L. Liu, ACS Appl. Mater. Interfaces 2023, 15, 5787.
- [21] Q. Chen, L. Huang, X. Wang, Y. Yuan, ACS Appl. Mater. Interfaces 2023, 15, 24901.
- [22] M. Zhu, X. Yan, X. Li, L. Dai, J. Guo, Y. Lei, Y. Xu, H. Xu, ACS Appl. Mater. Interfaces 2022, 14, 45697.
- [23] H. Gui, X. Zhao, S. Zuo, W. Liu, C. Wang, P. Xu, Y. Ding, C. Yao, ACS Appl. Mater. Interfaces 2023, 15, 39740.
- [24] T. Xue, Y. Yang, D. Yu, Q. Wali, Z. Wang, X. Cao, W. Fan, T. Liu, Nano-Micro Lett. 2023, 15, 45.
- [25] Y. Lu, X. Zhao, Y. Lin, P. Li, Y. Tao, Z. Wang, J. Ma, H. Xu, Y. Liu, Carbon 2023, 206, 375.
- [26] Z. Guo, P. Ren, F. Yang, T. Wu, L. Zhang, Z. Chen, S. Huang, F. Ren,
- ACS Appl. Mater. Interfaces 2023, 15, 7308.
  [27] M. Cheng, M. Ying, R. Zhao, L. Ji, H. Li, X. Liu, J. Zhang, Y. Li, X. Dong, X. Zhang, ACS Nano 2022, 16, 16996.
- [28] X. Bian, Z. Yang, T. Zhang, J. Yu, G. Xu, A. Chen, Q. He, J. Pan, ACS Appl. Mater. Interfaces 2023, 15, 41906.
- [29] L. Liang, Q. Li, X. Yan, Y. Feng, Y. Wang, H.-B. Zhang, X. Zhou, C. Liu, C. Shen, X. Xie, ACS Nano 2021, 15, 6622.
- [30] H. Wang, C. Ji, C. Zhang, Y. Zhang, Z. Zhang, Z. Lu, J. Tan, L. J. Guo, ACS Appl. Mater. Interfaces 2019, 11, 11782.
- [31] C. Yuan, J. Huang, Y. Dong, X. Huang, Y. Lu, J. Li, T. Tian, W. Liu, W.
- Song, ACS Appl. Mater. Interfaces 2020, 12, 26659.
  [32] Z.-y. Jiang, W. Huang, L.-s. Chen, Y.-h. Liu, Opt. Express 2019, 27, 24194
- [33] J. He, A. Li, W. Wang, C. Cui, S. Jiang, M. Chen, W. Qin, H. Tang, R.
- Guo, *Ind. Eng. Chem. Res.* **2023**, *62*, 9221. [34] T. Mai, W.-Y. Guo, P.-L. Wang, L. Chen, M.-Y. Qi, Q. Liu, Y. Ding, M.-G.
- Ma, Chem. Eng. J. 2023, 464, 142517.
- [35] V. V. Tran, D. D. Nguyen, A. T. Nguyen, M. Hofmann, Y.-P. Hsieh, H.-C. Kan, C.-C. Hsu, ACS Appl. Nano Mater. 2020, 3, 7474.
- [36] H. Fu, L. Chen, D. Liu, Y. Zhang, Y. Cao, C. Wu, Z. Yong, Y. Yu, Q. Li, Chem. Eng. J. 2023, 454, 140324.
- [37] D. Wanasinghe, F. Aslani, Compos. Part B: Eng. 2019, 176, 107207.
- [38] J. Kim, M. Li, O. Hinder, P. W. Leu, Adv Neural Inf Process Syst. 2024, 36.
- [39] J. Kim, M. Li, Y. Li, A. Gomez, O. Hinder, P. W. Leu, *Digital Discovery* 2024. 3, 381.
- [40] M. Li, M. J. McCourt, A. J. Galante, P. W. Leu, Opt. Express 2022, 30, 33182.
- [41] H. Wang, M. He, H. Liu, Y. Guan, ACS Appl. Mater. Interfaces 2019, 11, 25586.
- [42] Z. Jiang, S. Zhao, L. Chen, Y.-h. Liu, Opt. Express 2021, 29, 18760.
- [43] J. Gu, S. Hu, H. Ji, H. Feng, W. Zhao, J. Wei, M. Li, Nanotechnology 2020, 31, 185303.
- [44] X. Zhu, A. Guo, Z. Yan, F. Qin, J. Xu, Y. Ji, C. Kan, Nanoscale 2021, 13, 8067.
- [45] H. Yang, S. Bai, X. Guo, H. Wang, Appl. Surf. Sci. 2019, 483, 888.
- [46] T. Gao, P. W. Leu, Opt. Express 2013, 21, A419.
- [47] T. Gao, P. W. Leu, J. Appl. Phys. 2013, 114, 063107.
- [48] T. Gao, B. Wang, B. Ding, J.-K. Lee, P. W. Leu, Nano Lett. 2014, 14, 2105.
- [49] M. Li, M. Zarei, K. Mohammadi, P. W. Leu, ACS Appl. Mater. Interfaces 2023, 15, 30591.
- [50] H. Li, Y. Zhang, Y. Tai, X. Zhu, X. Qi, L. Zhou, Z. Li, H. Lan, Opt. Laser Technol. 2022, 148, 107717.
- [51] S.-i. Chung, T.-W. Kang, P. K. Kim, T.-g. Ha, Y.-P. Hong, ACS Appl. Mater. Interfaces 2023, 15, 56612.
- [52] Y. Han, Y. Liu, L. Han, J. Lin, P. Jin, Carbon 2017, 115, 34.



www.advancedsciencenews.com

www.advmattechnol.de

- [53] M. I. Kayes, M. M. Zarei, F. Feng, P. W. Leu, Nanotechnology 2023, 35, 025102.
- [54] M. Zarei, J. C. Loy, M. Li, Z. Zhou, S. Sinha, M. LeMieux, S. B. Walker, B. P. Rand, P. W. Leu, *Opt. Express* 2023, 31, 34697.
- [55] Q. Lei, Z. Luo, X. Zheng, N. Lu, Y. Zhang, J. Huang, L. Yang, S. Gao, Y. Liang, S. He, *Opt. Mater. Express* 2023, 13, 469.
- [56] H. Zhang, X. Zhu, J. Zhou, H. Li, Z. Li, L. Sun, R. Wang, F. Zhang, Q. Xu, J. Zhao, Y. Huang, W. Yang, G. Zhang, H. Lan, Adv. Mater. Technol. 2023, 8, 2201580.
- [57] L. Sun, R. Wang, X. Zhu, H. Li, J. Zhang, F. Wang, G. Zhang, J. Yang, Z. Peng, Y. Zhang, H. Lan, Adv. Mater. Technol. 2022, 7, 2200584.
- [58] R. K. Govind, I. Mondal, K. Baishya, M. K. Ganesha, S. Walia, A. K. Singh, G. U. Kulkarni, Adv. Mater. Technol. 2022, 7, 2101120.
- [59] J. Yang, D. Zi, X. Zhu, H. Li, Z. Li, L. Sun, G. Zhang, F. Wang, Z. Peng, H. Lan, Adv. Mater. Technol. 2022, 7, 2101087.
- [60] M. Zarei, M. Li, E. E. Medvedeva, S. Sharma, J. Kim, S. B. Walker, M. LeMieux, P. W. Leu, ACS Appl. Mater. Interfaces 2024, 16, 6382.
- [61] A. S. Voronin, Y. V. Fadeev, I. V. Govorun, I. V. Podshivalov, M. M. Simunin, I. A. Tambasov, D. V. Karpova, T. E. Smolyarova, A. V. Lukyanenko, A. A. Karacharov, I. V. Nemtsev, S. V. Khartov, J. Mater. Sci. 2021, 56, 14741.

- [62] S. Walia, A. K. Singh, V. S. G. Rao, S. Bose, G. U. Kulkarni, Bull. Mater. Sci. 2020, 43, 187.
- [63] D. Liao, Y. Zheng, X. Ma, Y. Fu, Opt. Express 2023, 31, 32200.
- [64] A. Voronin, Y. Fadeev, F. Ivanchenko, S. Dobrosmyslov, M. Makeev, P. Mikhalev, A. Osipkov, I. Damaratsky, D. Ryzhenko, G. Yurkov, M. Simunin, M. Volochaev, I. Tambasov, S. Nedelin, N. Zolotovsky, D. Bainov, S. Khartov, Surf. Interfaces 2023, 38, 102793.
- [65] M.-H. Kim, H. Joh, S.-H. Hong, S. J. Oh, Curr. Appl. Phys. 2019, 19, 8
- [66] A. S. Voronin, Y. V. Fadeev, M. O. Makeev, P. A. Mikhalev, A. S. Osipkov, A. S. Provatorov, D. S. Ryzhenko, G. Y. Yurkov, M. M. Simunin, D. V. Karpova, A. V. Lukyanenko, D. Kokh, D. D. Bainov, I. A. Tambasov, S. V. Nedelin, N. A. Zolotovsky, S. V. Khartov, *Materials* 2022, 15, 1449.
- [67] Z. Jiang, S. Zhao, W. Huang, L. Chen, Y.-h. Liu, Opt. Express 2020, 28, 26531.
- [68] J. Wang, Q. Hu, J. Huang, J. Li, Y. Lu, T. Liang, B. Shen, W. Zheng, W. Song, Adv. Mater. Interfaces 2022, 9, 2102322.
- [69] S. A. Mann, E. C. Garnett, Nano Lett. 2013, 13, 3173.
- [70] S. B. Walker, J. A. Lewis, J. Am. Chem. Soc. 2012, 134, 1419.